

Modeling Reactions on the Solid-Liquid Interface With Next Generation Extended Lagrangian Quantum-Based Molecular Dynamics

Rae A. Corrigan Grove,[†] Kevin G. Kleiner,[‡] Joshua D. Finkelstein,[‡] Ivana Gonzales,[†] Michael E. Wall,[¶] Travis E. L. Jones,[†] Anders M. N. Niklasson,[†] and Christian F. A. Negre^{*,†}

[†]*Theoretical Division, Los Alamos National Laboratory, Los Alamos, NM 87545*

[‡]*Computational Physics Division, Los Alamos National Laboratory, Los Alamos, NM 87545*

[¶]*Computer, Computational, and Statistical Sciences Division, Los Alamos National Laboratory, Los Alamos, NM 87545*

E-mail: cnegre@lanl.gov

1 Abstract

In this work, we demonstrate how extended Lagrangian Born-Oppenheimer quantum-based molecular dynamics (XL-BOMD) can be used to simulate heterogeneous electrocatalytic reactions. In particular, we apply our framework to study the oxygen reduction reaction (ORR) mechanism on nitrogen-doped graphene in an aqueous solution. The electronic ground state and total energy of XL-BOMD are stabilized through nuclear and electronic equations of motion assisted by an integral kernel updated with low-rank approximations. A species charge analysis reveals that the XL-BOMD simulations can be used to detect electron transfer between the catalyst surface and the solvated molecular oxygen mediated by water molecules, resulting in the molecular dissociation of O₂. Simulations of the ORR under high electrochemical biases contribute to a larger body of work elucidating an outer-sphere ORR mechanism in which reduction occurs through water networks without direct adsorption of molecular oxygen.

2 Introduction

As energy demands continue to grow, the development of cost-effective materials to facilitate efficient energy conversion is becoming increasingly important.^{1,2} The rate-limiting step in current fuel cell cathodes is the kinetically slow oxygen reduction reaction (ORR). Platinum group metals (PGM) are state-of-the-art catalysts for the ORR, but are costly and scarce, making them inadequate for large-scale applications.^{3,4} Promising alternative PGM-free catalysts include a variety of metal- and nitrogen-doped carbon materials, such as the nitrogen-doped graphene (NG) used in this study.^{5,6} NG is a promising candidate for a PGM-free catalyst because of its performance and availability. Due to its simplicity, this material provides a good framework for studying possible ORR mechanisms both experimentally and theoretically.⁷ Furthermore, the mechanistic details of the ORR catalyzed by NG have been the subject of extensive previous research,⁷⁻¹² providing a strong foundation for the new kind of theoretical studies presented here.

For these PGM-free catalysts, the role of

electrolyte in the charge transfer between the electrode and the active species is still under debate. The inner and outer-sphere ORR mechanisms have both been proposed, with the mechanism likely depending on the particular material.^{12,13} To design improved NG-based catalysts, we need to understand how the atomic configurations impact these mechanisms. Thus, a detailed atomistic modeling of the chemistry of the solid-liquid interface is needed before optimizing the atomic nature and arrangements of the surface for commercial applications.^{3,14} In this regard, theoretical approaches such as embedded interface clusters have proven successful in calculating geometries and adsorption binding energies to model processes at the ionic solid-water interface.¹⁵ Additionally, electronic structure-based methods such as quantum-based molecular dynamics (QMD) can be used to directly simulate the ORR. These simulations effectively sample the most energetically favorable configurations by integrating Newton’s equations of motion with forces computed quantum mechanically.^{16,17} In the context of heterogeneous catalysis, and in particular of oxygen reduction, first-principles QMD simulations have been successfully applied.^{9,18}

The accuracy and efficiency in the simulation of PGM-free catalysts are especially important, as the reaction mechanisms are highly dependent on the specific geometry of the active sites and their surroundings, as well as the charge transfer pathways at the catalyst-electrolyte interface.^{19,20} With the help of accurate predictive simulations, materials engineers can provide rational guidance for the design of optimal catalytic surfaces and electrolyte solutions for the ORR. Pioneering first-principles QMD simulations have suggested that carbon atoms directly connected to nitrogen atoms in the NG sheet constitute the active site.⁹ Other first principle studies have shown that the overpotential is significantly affected by the nitrogen density,²¹ while others have determined a strong influence of the corrugation of the sheet in addition to the nitrogen concentration.¹¹ Moreover, the relative position of N atoms within the graphene sheet appears to

have a significant influence on reaction free energy.²²

Most density functional theory (DFT) studies assume that the ORR proceeds via proton-coupled electron transfer (PCET). For example, a DFT-based study using the energetics of intermediates to explore plausible ORR pathways has shown that a direct four-electron pathway can occur on NG.²² This study assumes proton-coupled electron transfer steps via a pure inner-sphere mechanism, as mentioned above. Another DFT-based study describes possible mechanisms involving four- and two-electron pathways.²³ Although such studies contribute to obtaining a complete atomistic description of the ORR, experiments often claim that the rate-limiting step (on metallic electrodes) is the molecular oxygen activation, $\text{O}_2 + \text{e}^- \rightarrow \text{O}_2^-$;²⁴ a process that is difficult to simulate with traditional techniques. For cases where adsorption onto the catalyst surface activates molecular oxygen, the assumption of PCET remains valid. However, for a poor performing catalyst that requires high overpotentials, it could be possible that O_2 is activated by electron transfer through an outer-sphere mechanism, making the adsorption step less important. Based on the previous information, it should be possible to depict an outer-sphere mechanism (without the O_2 adsorption step) by simulating the ORR at conditions similar to those of high overpotentials. In fact, a recent DFT study on metal-NG catalysts has shown that ORR can proceed through an outer-sphere mechanism with hydrogen peroxide as an intermediate.¹²

Due to the complexity of surface catalytic reactions, especially when considering the solvent molecules, QMD constitutes a potentially reliable and useful tool requiring exploration. QMD methods are frequently based on the Born-Oppenheimer approximation,^{25–28} which separates nuclear and electronic degrees of freedom. This approximation uses the fact that electrons evolve on a much faster time scale than slow nuclear degrees of freedom, so that electrons always relax to their equilibrium state following any nuclear motion.²⁹ Unfortunately, calculating the electronic ground state den-

sity at each time step is rather computationally expensive.³⁰ The iterative self-consistent field (SCF) optimization needed to compute the ground-state density often requires repeated diagonalizations of the electronic Hamiltonian. In the case of catalytic solid-liquid interfaces with full solvation, SCF optimization can also have convergence problems due to the metallic-like behavior of the electronic structure of the catalyst, further increasing the computational cost and limiting the accessible time scale of QMD simulations.³¹

In the new generation of extended Lagrangian first-principles molecular dynamics (XL-BOMD) methods developed by Niklasson et al.,^{29,32–39} both the nuclear and extended electronic degrees of freedom are evolved. The electronic evolution follows a similar approach as in the Car-Parrinello QMD method.^{37,40} However, in contrast to Car-Parrinello, only a single full diagonalization of the electronic Hamiltonian is needed at each time step. Moreover, XL-BOMD avoids system-dependent electron mass parameters and allows longer integration time steps of the same order as in regular BOMD.^{29,37} The error of the sampled Born-Oppenheimer potential energy surface is of the fourth order in the integration time step with a small prefactor. This accuracy can be increased to the eighth order if necessary.³⁹ In XL-BOMD the electronic degrees of freedom evolve through a harmonic oscillator that closely follows the exact ground state during a QMD simulation. In its most recent incarnation, this oscillator includes an inner-product kernel which acts as a preconditioner,^{29,37,38} and can be efficiently approximated with a preconditioned low-rank Krylov subspace expansion.⁴¹

In this article, we test a recent formulation of XL-BOMD^{29,37} using a specific system of solvated molecular oxygen at the interface of a NG sheet. First, we verify the utility of the kernel in improving the initial convergence of the SCC optimization. We then perform XL-BOMD simulations for several picoseconds and show evidence of the oxygen reduction reaction with charge transfer occurring at the NG-water interface.

3 Methods

3.1 Density Functional Tight Binding Theory

Density functional theory (DFT) has been a primary workhorse for computational chemistry for the last three decades, as it is a relatively inexpensive technique for analyzing the energetics of simple molecules in vacuum and small crystal units.^{42–46} However, a time-resolved dynamics picture of chemical reactions including several hundreds to thousands of atoms has remained out of reach with direct DFT-based QMD simulations. In these QMD simulations, forces are evaluated for each new configuration, which has to be repeated over thousands of time steps, and first-principles DFT is therefore in general too expensive for most practical applications. Simplifying approximations are, therefore, needed to reduce the computational cost. The self-consistent charge density functional tight-binding theory (SCC-DFTB) provides a well-balanced approximation between speed and accuracy.^{47–49} SCC-DFTB is based on a second-order approximation of the Kohn-Sham energy functional in DFT with respect to fluctuations around a set of overlapping neutral atomic electron densities. The SCC-DFTB Kohn-Sham Hamiltonian can be written as:

$$H_{\mu\nu} = \langle \phi_\mu | \hat{H}_0 | \phi_\nu \rangle + \frac{1}{2} S_{\mu\nu} \sum_k (\gamma_{ik} + \gamma_{jk}) \Delta q_k \quad (1)$$

where ϕ_μ and ϕ_ν are atomic orbitals belonging to atoms i and j , respectively, and \hat{H}_0 is the non-SCC Hamiltonian operator.⁴⁷ S is the overlap matrix, where each value of the off-diagonal element $S_{\mu\nu}$ is given by the inner product $\langle \phi_\nu | \phi_\mu \rangle$. The last term contains the dependence on the fluctuation of the charge. γ_{ij} is a function that converges to 1.0 in the long-range limit, leading to a pure Coulombic potential produced by charges Δq_k . In the opposite case, when both orbitals are close to each other, γ_{ij} becomes $\gamma_{ii} = U_i$, where U is the Hubbard parameter that accounts for the self-interaction of electrons, which is related to the chemical hardness of the atomic species. Charge fluctuation

tuations $\Delta q_i = q_i - q_i^0$ are obtained from the Mulliken analysis:

$$\Delta q_i = \sum_{\nu \in i} \frac{1}{2} (S\rho + \rho S)_{\nu\nu} - z_i \quad (2)$$

where ρ is the density matrix, and z_i is the electron population of the isolated species i . The summation runs through every orbital ν that belongs to atom i . The density matrix is computed as $\rho = Cf(\epsilon)C^T$, where C is the matrix of the eigenvectors of H ; ϵ is the diagonal matrix containing the eigenvalues of H ; and $f(\epsilon)$ is the Fermi distribution function defined as $f(\epsilon) = 1/(1 + \exp(-\beta(\epsilon - \mu_e)))$, where β is the inverse electronic temperature and μ_e is the chemical potential for the electrons.

The SCC-DFTB method is appropriate for cases where there is a large charge redistribution^{47,50} and is faster than the regular Kohn-Sham DFT calculations by up to three orders of magnitude, often without significant loss of accuracy.⁵¹⁻⁵³ SCC-DFTB is implemented in the DFTB+⁴⁸ and LATTE⁵⁴ codes. In the LATTE code, the Hamiltonian elements are expressed as a decaying exponential of a polynomial function of the interatomic distances. The coefficients for the polynomial function depend on the nature of the orbitals and the species they belong to. A special characteristic of the LATTE Hamiltonian is the transferability. The new *lanl31* parametrization has proven to be highly transferable and has been used in studies involving different types of systems such as proteins,⁵⁵ high-explosives,^{56,57} and molecular crystals.⁵⁸ The code for performing the simulations in this work consists of a DFTB-based code that uses the LATTE Hamiltonian method.⁵⁵

3.2 Extended Lagrangian Born-Oppenheimer MD

Extended-Lagrangian Born-Oppenheimer MD guarantees a smooth evolution of the charge which appears as a dynamical field variable in the equations of motion. XL-BOMD also allows us to use a relatively long integration time step, as in regular Born-Oppenheimer MD, while

maintaining system stability. We will briefly present the XL-BOMD method as explained elsewhere.^{29,37} Regardless of the underlying level of theory, in regular Born-Oppenheimer molecular dynamics, the potential energy surface, $U_{\text{BO}}(\mathbf{R})$, with $\mathbf{R} = \{R_i\}_{i=1}^N$ being the nuclear coordinates, is determined through an iterative self-consistent optimization of a nonlinear energy function of the electron density or charge distribution. In XL-BOMD, $U_{\text{BO}}(\mathbf{R})$ is replaced by a *shadow*, or approximate, potential energy surface, $\mathcal{U}_{\text{BO}}(\mathbf{R}, n)$, which is based on the relaxed ground state of an approximate shadow energy functional that is based on a linearization of the regular energy density functional around an approximate ground state density $n(\mathbf{r})$, where \mathbf{r} are the electronic coordinates. Due to this linearization, the optimized density of the ground state, $\varrho[n(\mathbf{r})]$ is given directly through a single diagonalization, avoiding expensive iterations. The density in XL-BOMD, $n(\mathbf{r})$, is then included as a dynamic field variable that evolves through a harmonic oscillator that is centered around the exact density of the ground state, or the best approximation available to the exact ground state, that is, $\varrho[n(\mathbf{r})]$. In this way $\mathcal{U}_{\text{BO}}(\mathbf{R}, n(\mathbf{r}))$ closely follows the exact surface of the potential energy with an error that scales quadratically as $\mathcal{O}(\|\varrho[n(\mathbf{r})] - n(\mathbf{r})\|^2)$.³⁷ The accuracy of the shadow potential can be further improved by a first-level update³⁹ which has been used in these simulations.

The extended Lagrangian functional $L(\mathbf{R}, \dot{\mathbf{R}}, n, \dot{n})$ includes the nuclear kinetic energy, the *shadow* potential energy surface, the motion of the electron density, and a harmonic oscillator for the electron density centered around $\varrho[n(\mathbf{r})]$. The harmonic oscillator also includes a metric tensor, $T = K^T K$, given through an integral kernel K , which is defined as the inverse Jacobian of the residual function, $\varrho[n(\mathbf{r})] - n(\mathbf{r})$. This kernel keeps the density variable $n(\mathbf{r})$ oscillating close to the exact, fully optimized Born-Oppenheimer ground state density, $\rho_{\text{min}}(\mathbf{r})$.

In our XL-BOMD finite-dimensional DFTB-based formulation,^{37,59} the continuous charge density, $n(\mathbf{r})$, is represented by a set of net Mulliken charges, $\mathbf{n} = \{n_i\}_{i=1}^N$, where N is the total

number of atomic sites i in the system. The equations of motion for this DFTB-based XL-BOMD scheme govern the evolution of both the coarse-grained atomic charge distribution, \mathbf{n} , and the corresponding nuclear configuration, \mathbf{R} . These equations, derived from the classical adiabatic limit,^{37,38,59} are

$$\begin{aligned} M_i \ddot{R}_i &= - \left. \frac{\partial \mathcal{U}_{\text{BO}}(\mathbf{R}, \mathbf{q}[\mathbf{n}])}{\partial R_i} \right|_{\mathbf{n}}, \\ \dot{\mathbf{n}} &= -\omega^2 K(\mathbf{q}[\mathbf{n}] - \mathbf{n}). \end{aligned} \quad (3)$$

where M_i denotes the nuclear mass of atom i and $\mathbf{q}[\mathbf{n}] = \{q_i[\mathbf{n}]\}_{i=1}^N$ is a vector containing approximate ground state occupations for each atom that are given from the optimization of the linearized energy expression, that is, the coarse-grained Mulliken net charge version of $\varrho[n(\mathbf{r})]$ above. The nuclear equations of motion are integrated with the standard Verlet scheme, and the electronic equation of motion is integrated with a modified Verlet scheme that includes moderate dissipation terms^{37,60,61} that help to keep the electronic and nuclear degrees of freedom synchronized. At the first QMD time step, the extended dynamical variables for the electronic degrees of freedom, $\mathbf{n}(t_0)$, are set to the fully converged regular Born-Oppenheimer ground state densities. The deviation of charge from the exact ground state scales with the size of the integration time step, δt , as $\|\mathbf{q}[\mathbf{n}] - \mathbf{n}\| \propto \delta t^2$.³⁷

In the DFTB-based formalism for XL-BOMD, the kernel K is represented by an $N \times N$ matrix

$$K = \left(\left\{ \frac{\partial \mathbf{q}[\mathbf{n}]}{\partial n_i} \right\}_{i=1}^N - I \right)^{-1} = J^{-1}, \quad (4)$$

where $\{\partial \mathbf{q}[\mathbf{n}]/\partial n_i\}_{i=1}^N$ is a set of N column vectors each having length N containing occupation response derivatives per atom and J is the Jacobian matrix of the residual function. The kernel K appears as a preconditioner that acts on the residual function of Eq. (3) and keeps \mathbf{n} oscillating close to the exact fully-optimized density of the ground state. The kernel helps to keep the integration stable for simulations

involving highly reactive chemical systems. Recalculating the full inverse Jacobian matrix in Eq. (4) at each time step is computationally too expensive to be practical. We therefore simplify this matrix computation by using a rank- N update of a scaled delta function as an approximation of K .³⁷ The rank- N update can be calculated from quantum perturbation theory.⁶² Typically, $N \leq 4$ and is used during simulation based on residual error, $\mathbf{q}[\mathbf{n}] - \mathbf{n}$. If the residual error is still too large following a rank-4 update, the kernel is recalculated. In general, this adds little extra cost to each time step, but significantly improves the stability of the resulting molecular trajectories.

4 Results and Discussion

Here we apply the XL-BOMD simulation method using the low-rank updated kernel approximation to simulate the ORR. The idea behind this simulation is twofold: to verify the robustness and reliability of XL-BOMD as a valid simulation tool for reactive systems; and to shed light on details of the ORR as catalyzed by NG using high overpotential.

The main system configuration consisted of a 19.686 x 17.048 x 20.000 Å³ box containing: O₂, 164 water molecules (solvent), and the NG sheet. The NG sheet was set up along one face of the water box. A total of four nitrogen atoms were included in the NG sheet, each fully bound to carbon atoms. This system (622 atoms in total) is shown in Figure 1. Variants containing molecular oxygen in different environments were also constructed for comparison purposes. These variants are as follows: O₂ with NG, O₂ in water, and O₂ with pure graphene in water.

The simulations were run for 10 ps using a 0.1 fs time step and periodic boundary conditions. A Langevin thermostat was used to maintain a constant temperature of 300 K throughout the simulation⁶³ with a friction coefficient of $\gamma = 0.01 \text{ fs}^{-1}$. More accurate methods could be used for larger friction values and may be explored in future work.⁶⁴ Since these are potentially reactive systems, an electronic temperature of 0.025 [eV] / 8.617E-5 [eV/K] \simeq 290 K

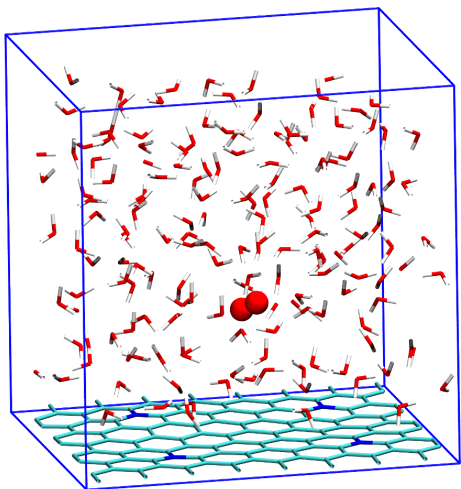


Figure 1: Full simulation system containing NG, O_2 , and water. Water molecules and the NG sheet are shown using a "dynamic bonds" representation with a cut-off of 1.8 Å, O_2 is shown as spheres. C, H, N, and O atoms are displayed in teal, white, blue, and red, respectively. The periodic bounding box (19.686 x 17.048 x 20.000 Å³) is shown in blue.

was used to "smear" the Fermi distribution and improve the stability of the QMD simulations. Rank- N updates to the kernel were performed with the maximum rank set to 4. Simulations were run on the Los Alamos National Laboratory Institutional Computing Chicoma supercomputing cluster, using a Nvidia A100 GPU for acceleration. Each time step took ~ 0.61 seconds wall-clock time using the GPMDK version that was available at the time production simulations were run.

Preconditioning was used with XL-BOMD to help improve the stability of the QMD simulations. Figure 2 shows the SCC iterations required for the initial convergence of the main system with and without preconditioning. This result demonstrates how preconditioning can greatly accelerate the SCC convergence required prior to MD simulation.

4.1 Mulliken Population Analysis

As mentioned in Section 3.1, the Mulliken populations need to be computed at every time step of the QMD simulations to compute the electronic structure. Although for most purposes, Mulliken populations are just auxiliary variables, they can be used to gauge the overall

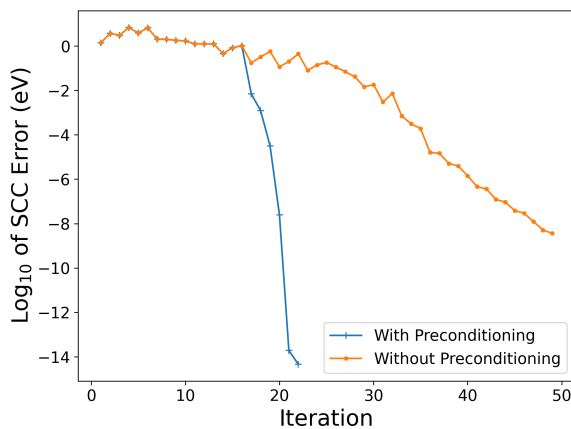


Figure 2: Logarithm of the SCC Error (in arbitrary units) as a function of the SCC iteration number. The results of using and not using preconditioning are shown in blue and orange, respectively. This figure shows the fast convergence attained when preconditioning (using a pre-calculated kernel) is used, which typically follows a second order power law ($\log_{10}(\text{Error}_i) \simeq 2 \log_{10}(\text{Error}_{i-1})$) beyond a sufficiently small (10^{-3}) SCF Error. This verification has been done for the case of NG with water and molecular oxygen.

charge of an atomic species. This total charge can also be used to characterize species in solutions with different total charges and oxidation states.

To characterize oxygen-related species of interest, we performed preliminary MD simulations and computed the average Mulliken population. Each simulation was run for 1 ps using the same setup described previously and each studied species was solvated in a 19.686 x 17.048 x 20.000 Å water box. Mulliken populations are shown in Table 1.

We can see a spread of values that range from hydroxide with a high population of 1.01 to molecular oxygen with a population of 0.00. This table contains species with oxidation states of 0 (O_2), I (H_2O_2 , HO_2^-), and II (H_2O , H_3O^+ , HO^-). Although there is no evident correlation between the oxidation state and the Mulliken population, we can still use the latter as a means of identifying aqueous oxygen-related species within the context of a complex MD system. In general, negatively charged species tended to have oxygen atoms with higher Mulliken populations. The "negative" oxygen in the hydroperoxide anion has

Table 1: Mulliken population for different aqueous oxygen species within the DFTB level of theory. These populations were computed based on MD simulations conducted with each species in a water box. For the case of peroxide anion, the oxygen of interest is depicted with bold fonts. Species are ordered based on mean population.

Species	Mean	Standard Deviation
HO^-	1.01	0.02
HOO^-	0.65	0.03
H_2O	0.65	0.01
HOO^-	0.46	0.05
H_3O^+	0.44	0.01
H_2O_2	0.32	0.01
O_2	0.00	0.01

a lower population compared to the oxygen in the hydroxide anion because of the presence of an additional HO in hydroperoxide which will remove electrons from the O-O bond. The population can also be quantitatively explained as each element -H, $-e^-$, $-\text{H}^+$, $-\text{OH}$, $-\text{O}^-$, $-\text{O}$, bringing approximately 0.325, 0.675, -0.200, -0.020, 0.135, and 0.000 population to oxygen, respectively.

4.2 MD Simulations

MD simulations for all previously described systems were run for 10 ps and results have been analyzed based on both geometry and Mulliken population analysis. No oxygen reduction was observed during the simulation timescale for any of the control systems. The system containing O_2 with pure graphene in water showed an initial slow electron injection, but no evidence of oxygen cleavage (Supplementary Figure S1). The results for all three control simulations are shown in the Supplementary Information (SI).

In contrast, for the main system (containing the three main components: NG, O_2 , and water), oxygen reduction was observed within two picoseconds of simulation time. Figure 3 shows a plot of the distance of the O-O bond versus the simulation time, demonstrating a clear cleavage of the O-O bond. The O-O bond cleavage occurs between approximately 0.9 and 1.04 ps. During this time, a sharp increase in the O-O separation distance is observed.

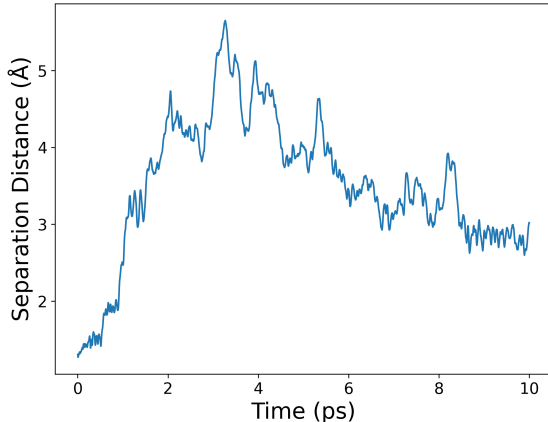


Figure 3: Distance between oxygen atoms in molecular oxygen as a function of time for a 10 ps QMD simulation. Between 0.9 and 1.04 ps, a sharp increase of O-O distance is clearly observed, demonstrating cleavage of the O-O bond.

Figure 4 shows the Mulliken populations of both molecular oxygen atoms as they undergo reduction (blue and orange). By direct comparison with Table 1 we can infer that the oxygen molecule transforms into HO^- (orange) and H_2O (blue) as a result of the reaction. The oxygen atom that is transformed into HO^- has a final Mulliken population similar to the average population shown in Table 1 for an HO^- oxygen. Analogously, the oxygen atom that is transformed into H_2O has a final Mulliken population similar to the average population shown in Table 1 for an H_2O oxygen. The sum of the Mulliken populations for all atoms in the NG sheet over the simulation time is shown in green on the same plot. Two important points are noticeable here: 1) A total of four electrons are transferred to the solution from the NG sheet, and, 2) The electron transfer proceeds in two steps. The final step can be clearly observed as a two-electron transfer beginning around 0.9 ps. The electrons that are not transferred directly to the molecular oxygen are transferred to water molecules which are reduced to form three additional hydroxide anions.

Figure 5 shows key frames of the simulation of the ORR with the NG catalyst. Molecular oxygen is shown as purple spheres for distinctiveness and the three water molecules that most directly participate in reduction are shown as

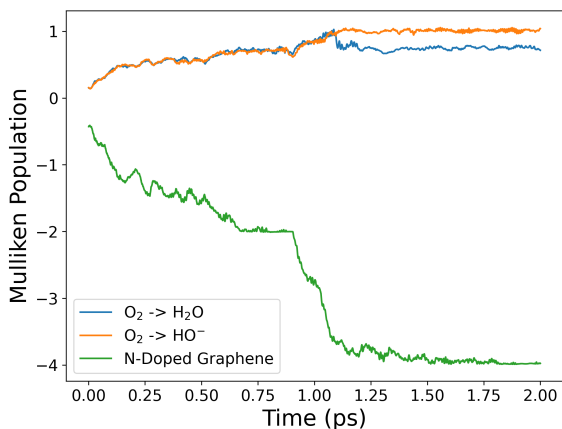


Figure 4: Mulliken populations for the two oxygen atoms that are initially part of the molecular oxygen molecule and the sum of Mulliken populations for all NG sheet atoms are shown. The Mulliken population of the oxygen atom from molecular oxygen that is reduced to form water is shown in blue and the Mulliken population of the oxygen atom from molecular oxygen that becomes a hydroxide anion is shown in orange. The sum of the Mulliken populations of all the atoms in the NG sheet is shown in green. Additional charge transferred from the NG sheet is going onto water oxygen atoms to form three additional HO^- anions (not shown). The identities of all molecular species were confirmed by VMD trajectory analysis.

red and white spheres (oxygen and hydrogen atoms, respectively). Bulk waters are shown as blue lines, while the NG sheet is shown as dynamic bonds with carbon and nitrogen atoms depicted in teal and blue, respectively. Frame A shows the initial configuration of the system, with the molecular oxygen atoms tightly bound (1.31 \AA separation distance). Frame B shows what appears to be the formation of a hydrogen peroxide-like intermediate with an O-O separation distance of 1.89 \AA . Comparison of oxygen charge populations at this point with the average Mulliken population values in Table 1 suggests that this intermediate is more similar to HOO^- than H_2O_2 . In addition, the injection of the first two electrons from the NG sheet is complete at this point. Frame C shows the formation of the first two HO^- ions. This point closely corresponds to the beginning of the second injection of electrons from the NG sheet as well. Frame D shows the formation of the final two HO^- ions and the single water molecule formed from one of the two initial molecular

oxygen atoms. In this last step, an OH^- picks up an H atom from neighboring water.

At the end of the simulation, O_2 is fully reduced to HO^- and water molecules. A total of 4 electrons were transferred from the NG catalyst to the solution. This electron transfer occurs under conditions of fully converged, self-consistent electronic structure.

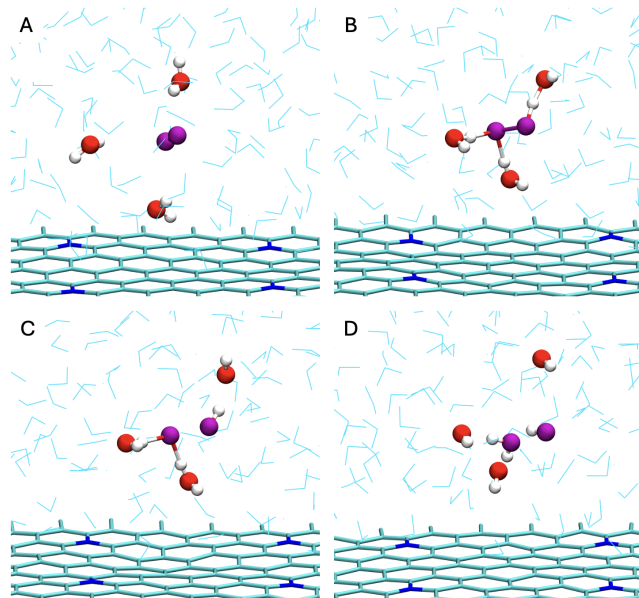


Figure 5: System configuration at simulation times of A) 0.000 ps, B) 0.894 ps, C) 0.939 ps D) 1.601 ps. C, N, H, and O atoms are depicted in teal, blue, white, and red colors respectively. The oxygen molecule is depicted in purple. Bulk waters are shown as light blue lines. For clarity, only 3 of the 164 water molecules are shown as spheres. Dynamic bonds shown are $\leq 1.8 \text{ \AA}$ in length, except for the O_2 bond, which is $\leq 2.0 \text{ \AA}$ in length.

Analysis of the final Mulliken population of the NG sheet reveals that the remaining positive charge (electron holes) is mostly located over the carbon atoms directly bonded to the doping nitrogen atoms (Supplementary Table S1).

Two extended systems were created by duplicating the main system in the x- or x- and y- directions to create larger NG sheets in proximity to more O_2 molecules. These simulations also showed evidence of ORR and electron transfer from the NG sheet through water (Supplementary Figures S2 and S3). A further description of these extended system simulations is available in the SI.

4.3 Additional Analysis

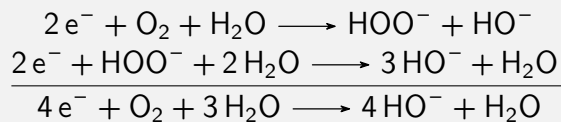
Two important elements of the electronic structure that can be monitored are the HOMO-LUMO energy gap and the residual error function. In this context, the HOMO is the highest occupied molecular orbital and the LUMO is the lowest unoccupied molecular orbital, also known as frontier orbitals. The residual error function is the norm of the difference between the exact ground state charge vector ($\rho[\mathbf{n}(\mathbf{r})]$) and the approximate charge vector ($\mathbf{n}(\mathbf{r})$) used as an auxiliary variable in the *shadow* energy function, as described in Section 3.2. It is important to note that this residual value is unique to the extended Lagrangian framework. Both of these elements can be used to identify reactions.

Figure 6 shows the HOMO-LUMO energy gap, residual function, NG Mulliken population sum, and O-O separation distance over simulation time. It is known that when reactions occur, the HOMO-LUMO gap tends to close (i.e., has a value near zero).⁶⁵ At two clear points during simulation (0.115 ps and 1.040 ps), the gap drops near zero. These coincide with the two waves of electrons that are injected into the solution from the NG sheet. It is important to note that the O-O bond does not cleave until the second pair of electrons is injected into the catalyst, as previously analyzed in Figure 3. These simulations were performed with zero bias. The HOMO-LUMO gap behavior may be different when a potential bias is applied.

As mentioned above, the residual value within the context of XL-BOMD can be used to identify reactions. The residual function increases when reactions occur.²⁹ Although not as clean as the HOMO-LUMO gap closing, we can see that at the two points at which the HOMO-LUMO gap nears zero, the residual function becomes large. Panels A, B, and C correspond to time points A, B, and C on the plot in Figure 6. These time points show critical configurations of the system, with A and C corresponding to the points where the HOMO-LUMO gap goes to zero.

After considering all the observations above, we can deduce that the ORR mechanism ob-

served in the simulation in two steps as follows:



The formation of an intermediate hydroperoxide anion in the simulations as part of the observed outer-sphere mechanism is probably due to the limitations of the simulation conditions, where there is no constant applied bias across the surface-electrolyte interface. The NG catalyst undergoes an oxidation, on the basis of evidence discussed above. This oxidation ($\text{NG} \longrightarrow \text{NG}^{4+} + 4e^-$) leads to four electron holes (net positive charges) in the NG sheet. This high capacitive charge could also contribute to the observation of an outer-sphere mechanism for the ORR.

The resulting electron holes are mostly localized over the carbon atoms directly bonded to the N atoms (Supplementary Table S1). As a possible explanation for the above, we have proposed the resonance structures shown in Figure 7. In these structures, we see that the holes are positioned such that they could be delocalized across the entire NG sheet.

From these computational experiments, we have shown that under simulation conditions NG is a more active catalyst than pure graphene. This can be explained by looking at the density of states (DOS) around the chemical potential of the electrons μ_e (Fermi level) for both materials. From Figure 8, we can see the DOS of O_2 (blue), carbon atoms near nitrogen doping atoms in NG (green), and pure graphene (red). Vertical lines indicating the positions of μ_e values for both material are also shown. The black dotted line indicates the LUMO state of O_2 that is susceptible to being filled with electrons upon reduction.

Both graphene and NG have states with electrons that can be donated to O_2 . However, in comparison to pure graphene, we can see that the effect of nitrogen doping is twofold - shifting μ_e to increase the reduction potential and increasing the density of states around μ_e , facilitating the source of electrons. This positive

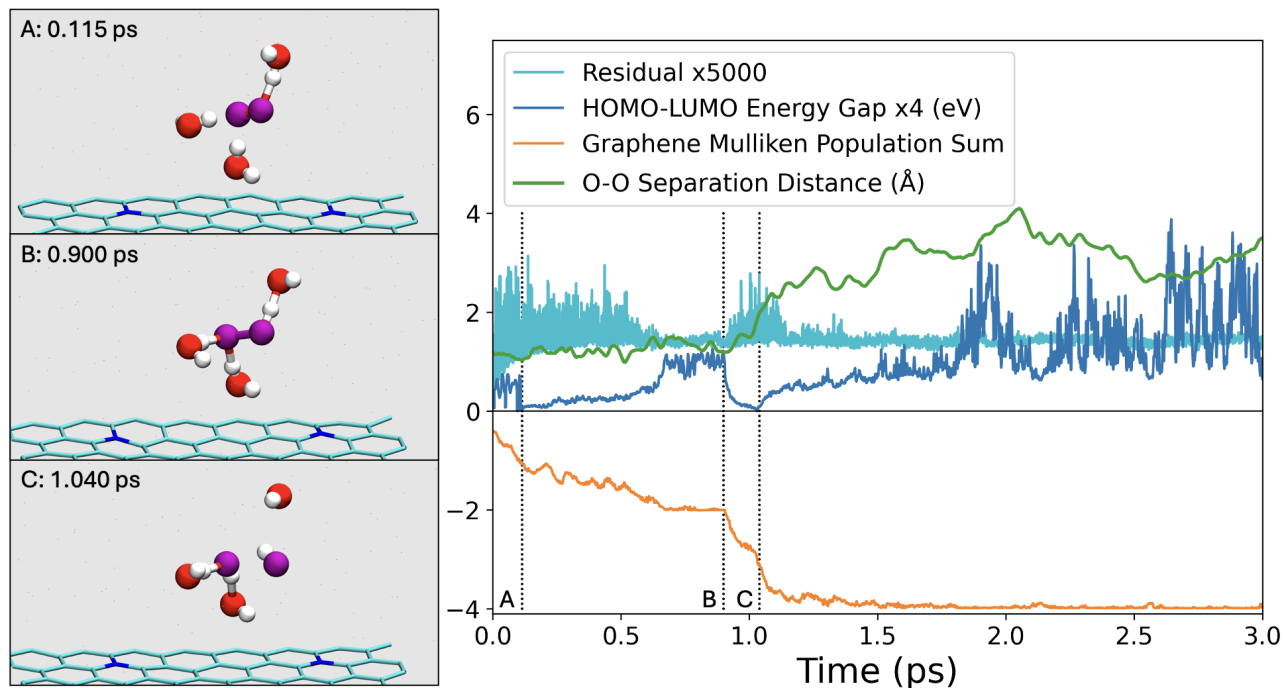


Figure 6: Overlay of four plots: residual ($q[n] - n$) multiplied by 5000 to show features (teal), HOMO-LUMO energy gap multiplied by 4 to show features (blue), separation distance between the two oxygen atoms that originally form molecular oxygen (green), and the sum of NG sheet atom Mulliken populations (orange). Panels A, B, and C to the left correspond to lines A, B, and C on the plot.

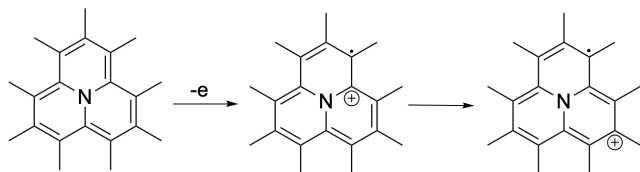


Figure 7: Possible resonance structures to explain the localization of the holes (positive charges) on the carbon atoms surrounding nitrogen doping atoms in the NG catalyst following oxidation. Mulliken population averages of nitrogen atoms and neighboring carbon atoms are available in Supplementary Table S1.

change in the value of μ_e is shown in Figure 8 as the difference between the green and red vertical lines.

It is known that pure graphene and NG have different potentials of zero charge and therefore different values of μ_e in the absence of charge, as evidenced in Figure 8. These QMD simulations are not performed under any constant applied external μ_e as it would be the case in an experimental setup. Given this limitation, it is possible that our simulations translate to a scenario where the applied $\mu_e(\text{NG})$ is higher than the applied μ_e (graphene), thus explaining the difference in reactivity.

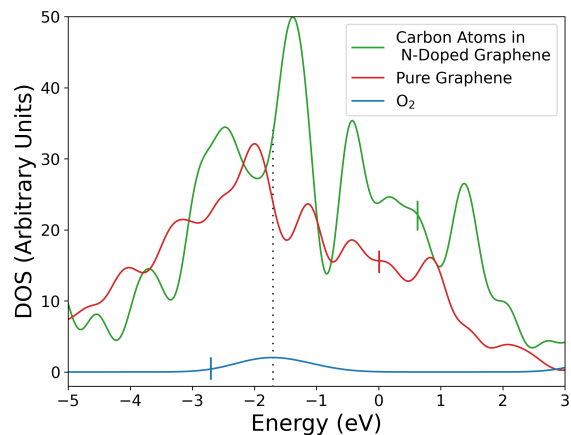


Figure 8: Total DOS for O_2 and pure graphene are shown along with the DOS corresponding to the carbon atoms bound to nitrogen dopant atoms in NG. Short vertical bars indicate the respective electron chemical potential (μ_e) values. The black dotted line shows the LUMO state of O_2 molecule. The plots were shifted so that μ_e of pure graphene is set to zero.

Another important point to note in these simulations is that the oxygen molecule does not need to be chemisorbed onto the NG sheet to undergo reduction. Reduction occurs via an outer-sphere mechanism mediated by the solvent molecules. The water molecules would act as nanowires allowing charge to flow between the catalytic surface and the O₂ molecule.⁶⁶ At the beginning of the simulation, the driving force for electron injection is the difference between $\mu_e(\text{NG})$ and $\mu_e(\text{solution})$. This difference is about 3.4 eV (Supplementary Table S2). From this we can deduce that a bias with a similar magnitude should be applied to refill the positive charges accumulated on the NG sheet following the ORR to maintain a steady-state process. From the analysis above, we can infer that the observed mechanism is most likely due to simulation conditions that translate to high-overpotential experimental conditions.

Although what was depicted here is not a formal electrochemical reaction due to the lack of steady-state current flowing through the system, we were still able to capture a full ORR. We were able to see that the catalytic material was formally oxidized upon the cleavage of molecular oxygen. There is a clear "redox" reaction occurring through an outer-sphere mechanism, with molecular oxygen and NG sheet being the oxidizing and reducing agents, respectively.

5 Conclusions

We have shown that the XL-BOMD simulation method based on DFTB can provide useful insight into the mechanism of electrocatalytic reactions beyond the energetic predictions of static DFT. This approach simultaneously maintains the charge distribution near the Born-Oppenheimer ground state and avoids performing expensive SCC optimizations at each time step. This advantage allows XL-BOMD to efficiently simulate large, highly reactive systems such as solid-liquid interfaces with first-principles accuracy. The electron transfer responsible for O₂ dissociation was directly captured by tracking the time evolution of the Mul-

liken populations as the reaction proceeded.

These studies suggest that, under current simulation conditions, which could translate to high overpotentials, the oxygen molecule does not need to be chemically adsorbed to the surface, and the ORR can proceed using an outer-sphere electron transfer mechanism. It is also possible that the outer-sphere mechanism is reflecting the fact that under current conditions, the catalyst acts like an ideally polarizable electrode. Follow-up studies will focus on including the possibility of simulating a steady-state current flowing through the catalytic surface-electrolyte interface. This will allow for better comparisons with previous experimental work. This will require updates to the QMD method to allow voltage application across the catalytic interface. Future work could also explore the role of H⁺ or OH⁻ ions in the solvent, as they relate to charge transfer mechanisms and bond break / formation resulting in the full O₂ reduction. Sheet defects with varying dopants can also be studied to learn their role in the O₂ reduction mechanism. Additionally, studying the ORR with bilayers in which a more inert layer such as pure graphene could be used to protect the catalytic surface could yield additional insights.

This work is only the first step in optimizing XL-BOMD simulation method for use with highly reactive systems, laying the groundwork for future studies and improvements. Using QMD simulations to develop a clear understanding of the structure-function relationships in chemically reactive catalytic systems can ultimately lead to the design of more efficient hydrogen fuel cells using PGM-free materials, such as the N-doped graphene studied here.

Acknowledgements

The work was performed at Los Alamos National Laboratory (LANL) in New Mexico. This article has been approved for unlimited distribution with the following assigned LA-UR number: 'LA-UR-25-20884'. This work was supported by the LANL LDRD-ER program; the Department of Energy Offices of Ba-

sic Energy Sciences (Grant No. LANLE8AN); and the Exascale Computing Project (17-SC-20-SC), a collaborative effort of two U.S. Department of Energy organizations (Office of Science and the National Nuclear Security Administration) responsible for the planning and preparation of a capable exascale ecosystem, including software, applications, hardware, advanced system engineering, and early testbed platforms, in support of the nation’s exascale computing imperative. Simulations were performed using Institutional Computing machines at LANL, supported by the US Department of Energy. LANL is operated by Triad National Security, LLC, for the National Nuclear Security Administration of the U.S. Department of Energy Contract No. 892333218NCA000001.

References

- (1) Morozan, A.; Jusselme, B.; Palacin, S. Low-platinum and platinum-free catalysts for the oxygen reduction reaction at fuel cell cathodes. *Energy Environ. Sci.* **2011**, *4*, 1238–1254.
- (2) Matanovic, I.; Artyushkova, K.; Atanassov, P. Understanding PGM-free catalysts by linking density functional theory calculations and structural analysis: Perspectives and challenges. *Curr. Opin. Electrochem.* **2018**, *9*, 137–144.
- (3) Song, C.; Zhang, J. In *PEM Fuel Cell Electrocatalysts and Catalyst Layers: Fundamentals and Applications*; Zhang, J., Ed.; Springer London: London, 2008; pp 89–134.
- (4) Marković, N. M.; Schmidt, T. J.; Stamenković, V.; Ross, P. N. Oxygen Reduction Reaction on Pt and Pt Bimetallic Surfaces: A Selective Review. *Fuel Cells* **2001**, *1*, 105–116.
- (5) Reyimjan, A. S.; Alfred, B. A.; Nalini, P. S.; Swaminatha, P. K.; Branko, N. P. O₂ Reduction on Graphite and Nitrogen-Doped Graphite: Experiment and Theory. *J. Phys. Chem. B.* **2006**, *110*, 1787–1793.
- (6) Yang, L.; Shui, J.; Du, L.; Shao, Y.; Liu, J.; Dai, L.; Hu, Z. Carbon-Based Metal-Free ORR Electrocatalysts for Fuel Cells: Past, Present, and Future. *Advanced Materials* **2019**, *31*, 1804799.
- (7) Ma, R.; Wang, K.; Li, C.; Wang, C.; Habibi-Yangjeh, A.; Shan, G. N-doped graphene for electrocatalytic O₂ and CO₂ reduction. *Nanoscale Adv.* **2022**, *4*, 4197–4209.
- (8) Ganyecz, A.; Kállay, M. Oxygen reduction reaction on N-doped graphene: Effect of positions and scaling relations of adsorption energies. *J. Phys. Chem. C Nanomater. Interfaces* **2021**, *125*, 8551–8561.
- (9) Okamoto, Y. First-principles molecular dynamics simulation of O₂ reduction on nitrogen-doped carbon. *Appl. Surf. Sci.* **2009**, *256*, 335–341.
- (10) Man, I.-C.; Trancă, I.; Soriga, S.-G. First principle studies of oxygen reduction reaction on N doped graphene: Impact of N concentration, position and co-adsorbate effect. *Appl. Surf. Sci.* **2020**, *510*, 145470.
- (11) Boukhvalov, D. W.; Son, Y.-W. Oxygen reduction reactions on pure and nitrogen-doped graphene: a first-principles modeling. *Nanoscale* **2012**, *4*, 417–420.
- (12) Low, J. L.; Roth, C.; Paulus, B. Exploring the Inner- and Outer-Sphere Mechanistic Pathways of ORR on M-N-Cs with Pyrrolic MN₄ Motifs. *J. Phys. Chem. C.* **2024**, *128*, 5075–5083.
- (13) Ramaswamy, N.; Mukerjee, S. Influence of Inner- and Outer-Sphere Electron Transfer Mechanisms during Electrocatalysis of Oxygen Reduction in Alkaline Media. *J. Phys. Chem. C.* **2001**, *115*, 18015–18026.
- (14) Jiao, Y.; Zheng, Y.; Jaroniec, M.; Qiao, S. Z. Origin of the Electrocatalytic

- Oxygen Reduction Activity of Graphene-Based Catalysts: A Roadmap to Achieve the Best Performance. *J. Am. Chem. Soc.* **2014**, *136*, 4394–4403.
- (15) Stefanovich, E. V.; Truong, T. N. A theoretical approach for modeling reactivity at solid-liquid interfaces. *J. Chem. Phys.* **1997**, *106*, 7700–7705.
- (16) Marx, D.; Hutter, J. *Ab Initio Molecular Dynamics: Basic Theory and Advanced Methods*; Cambridge University Press, 2009.
- (17) Vidossich, P.; Lledós, A.; Ujaque, G. First-Principles Molecular Dynamics Studies of Organometallic Complexes and Homogeneous Catalytic Processes. *Acc. Chem. Res.* **2016**, *49*, 1271–1278.
- (18) He, Y.; Chen, C.; Yu, H.; Lu, G. First principle molecular dynamics simulations of oxygen reduction reaction on Pt(111) in aqueous environment. *Catal. Commun.* **2016**, *87*, 74–77.
- (19) Ikeda, T.; Boero, M.; Huan, S.-F.; Terakura, K.; Oshima, M.; Ozaki, J.-I. Carbon Alloy Catalysts: Active Sites for Oxygen Reduction Reaction. *Phys. Stat. Sol.* **2008**, *112*, 14706–14709.
- (20) Holby, E. F.; Zelenay, P. Linking structure to function: The search for active sites in non-platinum group metal oxygen reduction reaction catalysts. *Nanoen.* **2016**, *29*, 54–64.
- (21) Wang, D.; Hu, J.; Wei, J.; Liu, X.; Hou, H. Insights into Nitrogen-doped Carbon for Oxygen Reduction: The Role of Graphitic and Pyridinic Nitrogen Species. *ChemPhysChem* **2023**, *24*, e202200734.
- (22) Zhang, L.; Xia, Z. Mechanisms of oxygen reduction reaction on nitrogen-doped graphene for fuel cells. *J. Phys. Chem. C Nanomater. Interfaces* **2011**, *115*, 11170–11176.
- (23) Yu, L.; Pan, X.; Cao, X.; Hu, P.; Bao, X. Oxygen reduction reaction mechanism on nitrogen-doped graphene: A density functional theory study. *J. Catal.* **2011**, *282*, 183–190.
- (24) Schmikler, W.; Santos, E. *Interfacial Electrochemistry*, 2nd ed.; Springer Berlin, Heidelberg, 2010.
- (25) Born, M.; Oppenheimer, R. J. Zur Quantentheorie der Molekeln. *Annalen der Physik* **1927**, *389*, 457–484.
- (26) Marx, D.; Hutter, J. In *Modern Methods and Algorithms of Quantum Chemistry*; Grotendorst, J., Ed.; John von Neumann Institute for Computing, 2000; 2nd edn.
- (27) Zhu, Z.; Tuckerman, M. E. Ab Initio Molecular Dynamics Investigation of the Concentration Dependence of Charged Defect Transport in Basic Solutions via Calculation of the Infrared Spectrum. *J. Phys. Chem. B* **2002**, *106*, 8009–8018.
- (28) Heitler, W.; London, F. Wechselwirkung neutraler Atome und homöopolare Bindung nach der Quantenmechanik. *Z. Physik* **1927**, *44*, 455–472.
- (29) Niklasson, A. M. Extended Lagrangian Born-Oppenheimer molecular dynamics: from density functional theory to charge relaxation models. *Eur. Phys. J. B* **2021**, *94*.
- (30) Rabuck, A. D.; Scuseria, G. E. Improving self-consistent field convergence by varying occupation numbers. *J. Chem. Phys.* **1999**, *110*, 695–696.
- (31) Kudin, K. N.; Scuseria, G. E. A black-box self-consistent field convergence algorithm: One step closer. *Phys. Rev. Lett.* **2002**, *116*, 8255–8256.
- (32) Niklasson, A. M. N. Extended Born-Oppenheimer Molecular Dynamics. *Phys. Rev. Lett.* **2008**, *100*, 123004.

- (33) Niklasson, A. M. N.; Tymczak, C. J.; Challacombe, M. Time-Reversible Born-Oppenheimer Molecular Dynamics. *Phys. Rev. Lett.* **2006**, *97*, 123001.
- (34) Cawkwell, M. J.; Niklasson, A. M. N. Energy conserving, linear scaling Born-Oppenheimer molecular dynamics. *J. Chem. Phys.* **2012**, *137*, 134105.
- (35) Souvatzis, P.; Niklasson, A. M. N. Extended Lagrangian Born-Oppenheimer molecular dynamics in the limit of vanishing self-consistent field optimization. *J. Chem. Phys.* **2013**, *139*, 214102.
- (36) Negre, C. F. A.; Mniszewski, S. M.; Cawkwell, M. J.; Bock, N.; Wall, M. E.; Niklasson, A. M. N. Recursive Factorization of the Inverse Overlap Matrix in Linear-Scaling Quantum Molecular Dynamics Simulations. *J. Chem. Theory Comput.* **2016**, *12*, 3063–3073.
- (37) Niklasson, A. M. N. Next generation extended Lagrangian first principles molecular dynamics. *J. Chem. Phys.* **2017**, *147*, 1–5.
- (38) Niklasson, A. M. N.; Cawkwell, M. J. Generalized extended Lagrangian Born-Oppenheimer molecular dynamics. *J. Chem. Phys.* **2014**, *141*, 1–5.
- (39) Niklasson, A. M. N.; Negre, C. F. A. Shadow energy functionals and potentials in Born-Oppenheimer molecular dynamics. *The Journal of Chemical Physics* **2023**, *158*, 154105.
- (40) Car, R.; Parrinello, M. Unified Approach for Molecular Dynamics and Density-Functional Theory. *Phys. Rev. Lett.* **1985**, *55*, 2471–2474.
- (41) Niklasson, A. M. N. Extended Lagrangian Born-Oppenheimer molecular dynamics using a Krylov subspace approximation. *J. Chem. Phys.* **2020**, *152*, 104103.
- (42) Parr, R. G.; Yang, W. *Density-functional theory of atoms and molecules*; Oxford University Press: Oxford, 1989.
- (43) Jones, R. O.; Gunnarsson, O. The density functional formalism, its applications and prospects. *Rev. Mod. Phys.* **1989**, *61*, 689–746.
- (44) Hohenberg, P.; Kohn, W. Inhomogeneous Electron Gas. *Phys. Rev.* **1964**, *136*, B864–B870.
- (45) Clark, A. E.; Adams, H.; Hernandez, R.; Krylov, A. I.; Niklasson, A. M. N.; Sarupria, S.; Wang, Y.; Wild, S. M.; Yang, Q. The Middle Science: Traversing Scale In Complex Many-Body Systems. *ACS Cent Sci* **2021**, *7*, 1271–1287.
- (46) Haunschild, R.; Barth, A.; French, B. A comprehensive analysis of the history of DFT based on the bibliometric method RPYS. *J. Cheminform.* **2019**, *11*, 72.
- (47) Elstner, M.; Porezag, D.; Jungnickel, G.; Elsner, J.; Haugk, M.; Frauenheim, T.; Suhai, S.; Seifert, G. Self-consistent-charge density-functional tight-binding method for simulations of complex materials properties. *Phys. Rev. Lett.* **1998**, *58*, 7260–7263.
- (48) Aradi, B.; Hourahine, B.; Frauenheim, T. DFTB+, a Sparse Matrix-Based Implementation of the DFTB Method. *J. Phys. Chem. A* **2007**, *111*, 5678–5684, PMID: 17567110.
- (49) Hourahine, B.; Aradi, B.; Blum, V.; Bonafé, F.; Buccheri, A.; Camacho, C.; Cevallos, C.; Deshayé, M. Y.; Dumitrică, T.; Dominguez, A.; Ehlert, S.; Elstner, M.; van der Heide, T.; Hermann, J.; Irle, S.; Kranz, J. J.; Köhler, C.; Kowalczyk, T.; Kubař, T.; Lee, I. S.; Lutsker, V.; Maurer, R. J.; Min, S. K.; Mitchell, I.; Negre, C.; Niehaus, T. A.; Niklasson, A. M. N.; Page, A. J.; Pecchia, A.; Penazzi, G.; Persson, M. P.; Řezáč, J.; Sánchez, C. G.; Sternberg, M.; Stöhr, M.; Stuckenberg, F.; Tkatchenko, A.; Yu, V. W.-z.; Frauenheim, T. DFTB+, a software package for efficient approximate density

- functional theory based atomistic simulations. *The Journal of Chemical Physics* **2020**, *152*, 124101.
- (50) Frauenheim, T.; Seifert, G.; Elsterner, M.; Hajnal, Z.; Jungnickel, G.; Porezag, D.; Suhai, S.; Scholz, R. A Self-Consistent Charge Density-Functional Based Tight-Binding Method for Predictive Materials Simulations in Physics, Chemistry and Biology. *Phys. Stat. Sol.* **2000**, *217*, 41–43.
- (51) Cui, Q.; Elstner, M.; Kaxiras, E.; Frauenheim, T.; Karplus, M. A QM/MM Implementation of the Self-Consistent Charge Density Functional Tight Binding (SCC-DFTB) Method. *J. Phys. Chem. B* **2000**, *105*, 569–585.
- (52) Elstner, M.; Jalkanen, K. J.; Knapp-Mohammady, M.; Frauenheim, T.; Suhai, S. Energetics and structure of glycine and alanine based model peptides: Approximate SCC-DFTB, AM1 and PM3 methods in comparison with DFT, HF and MP2 calculations. *J. Phys. Chem. B* **2001**, *263*, 203–219.
- (53) Krishnapriyan, A.; Yang, P.; Niklasson, A. M. N.; Cawkwell, M. J. Numerical Optimization of Density Functional Tight Binding Models: Application to Molecules Containing Carbon, Hydrogen, Nitrogen, and Oxygen. *J. Chem. Theory Comput.* **2017**, *13*, 6191–6200.
- (54) Bock, N.; Cawkwell, M. J.; Coe, J. D.; Krishnapriyan, A.; Kroonblawd, M. P.; Lang, A.; Liu, C.; Martinez Saez, E.; Mniszewski, S. M.; Negre, C. F. A.; Niklasson, A. M. N.; Sanville, E.; Wood, M. A.; Yang, P. LATTE. 2008; <https://github.com/lanl/LATTE>.
- (55) Negre, C. F. A.; Wall, M. E.; Niklasson, A. M. N. Graph-based quantum response theory and shadow Born–Oppenheimer molecular dynamics. *The Journal of Chemical Physics* **2023**, *158*, 074108.
- (56) Perriot, R.; Negre, C. F. A.; McGrane, S. D.; Cawkwell, M. J. Density functional tight binding calculations for the simulation of shocked nitromethane with LATTE-LAMMPS. *AIP Conf. Proc.* **2018**, *1979*, 050014.
- (57) Cawkwell, M. J.; Perriot, R. Transferable density functional tight binding for carbon, hydrogen, nitrogen, and oxygen: Application to shock compression. *The Journal of Chemical Physics* **2019**, *150*, 024107.
- (58) Singh, H.; Negre, C. F. A.; Redondo, A.; Perriot, R. Surface studies of beta-1,3,5,7-tetranitro-1,3,5,7-tetraoctane and pentaerythritol tetranitrate from density functional tight-binding calculations and implications on crystal shape. *Cryst. Growth Des.* **2024**, *24*, 3681–3690.
- (59) Aradi, B.; Niklasson, A. M. N.; Frauenheim, T. Extended Lagrangian Density Functional Tight-Binding Molecular Dynamics for Molecules and Solids. *J. Chem. Theory Comput.* **2015**, *11*, 3357–3363.
- (60) Niklasson, A. M. N.; Steneteg, P.; Odell, A.; Bock, N.; Challacombe, M.; Tymczak, C. J.; Holmström, E.; Zheng, G.; Weber, V. Extended Lagrangian Born-Oppenheimer molecular dynamics with dissipation. *J. Chem. Phys.* **2009**, *130*, 214109.
- (61) Zheng, G.; Niklasson, A. M. N.; Karplus, M. Lagrangian formulation with dissipation of Born-Oppenheimer molecular dynamics using the density-functional tight-binding method. *J. Chem. Phys.* **2011**, *135*, 044122.
- (62) Niklasson, A. M. N.; Cawkwell, M. J.; Rubensson, E. H.; Rudberg, E. Canonical density matrix perturbation theory. *Phys. Rev. E* **2015**, *92*, 1–2.
- (63) Sivak, D. A.; Chodera, J. D.; Crooks, G. E. Time Step Rescaling Recovers Continuous-Time Dynamical Properties for Discrete-Time Langevin Integration of Nonequilibrium Systems.

The Journal of Physical Chemistry B **2014**, *118*, 6466–6474, PMID: 24555448.

- (64) Finkelstein, J.; Cheng, C.; Fiorin, G.; Seibold, B.; Grønbech-Jensen, N. Bringing discrete-time Langevin splitting methods into agreement with thermodynamics. *The Journal of Chemical Physics* **2021**, *155*.
- (65) Bredas, J.-L. Mind the gap! *Mat. Horiz.* **2014**, *1*, 17–19.
- (66) Negre, C. F. A.; Jara, G. E.; Vera, D. M. A.; Pierini, A. B.; Sánchez, C. G. Detailed analysis of water structure in a solvent mediated electron tunneling mechanism. *J. Phys.: Condens. Matter* **2011**, *23*, 245305.

Supplementary Information

Supporting information for: Modeling Reactions on the Solid-Liquid Interface With Next Generation Extended Lagrangian Quantum-Based Molecular Dynamics

Control Systems

Three control systems were run to compare with the simulation results for the main system. The variant control systems are as follows: O_2 with N-doped graphene (NG), O_2 in water, and O_2 with carbon-only graphene (CG) in water. The starting coordinates for all three control systems were taken as pieces of the main system. The simulations were run for 10 ps using 0.1 fs time steps. A Langevin thermostat was used to maintain a simulation temperature of 300K and an electronic temperature corresponding to 0.025 eV to smear the Fermi distribution and improve stability. These simulation conditions match exactly the simulation conditions of the main system to ensure the most direct comparison. The ORR was not observed in any of the control systems in the tested time range. This is in contrast to the observation of the ORR in the main system after less than 2 ps. Plots of the Mulliken population of molecular oxygen atoms

over simulation time for the control systems and the main system are shown in Supplementary Figure S1. It is clear that the molecular oxygen atoms in the control simulations do not undergo reduction to form HO^- ions, since their Mulliken populations remain under 1.0 throughout the simulation time. In contrast, the oxygen atoms that initially form molecular oxygen in the main system are rapidly reduced to form HO^- and H_2O .

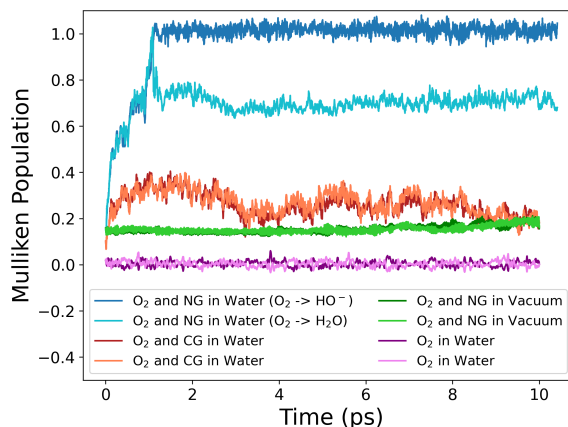


Figure S1: Mulliken populations for oxygen atoms that initially make up molecular oxygen across each of four simulations. In the main system, O_2 is reduced to form HO^- and H_2O , while in the control systems, the initial O_2 molecules remain intact. Difference in Mulliken populations between the control systems can be attributed to the presence of differing additional species (i.e., water, NG, and/or CG) in each system. Slight variations in the Mulliken populations for the control systems across time can be attributed to changes in interactions with or in proximity to those additional species (e.g., the slight increase in Mulliken population for the O_2 atoms in the last 2 ps of the O_2 with NG in vacuum simulation is due to O_2 moving closer to the NG sheet).

Extended Systems

To test the robustness of the XL-BOMD method in simulating ORR catalysis, various extended systems were constructed by replicating the entire system along an axis to obtain a larger NG-water interface with additional O_2 molecules. Both extended systems were simulated according to the same protocol using 0.1 fs time steps, a Langevin thermostat with a temperature of 300K, and an electronic tempera-

ture corresponding to 0.025 eV to smear the Fermi distribution and improve stability. Rank- N updates were performed with $N=4$.

Two systems were created by replicating the original system along the x- or x- and y- axes. These replicates extended the NG sheet and added additional O_2 molecules to the system. The first system was created by adding a single additional replica, which doubled the size of the system. The ORR was observed for one of the O_2 molecules after ~ 2.5 ps (Figure S2).

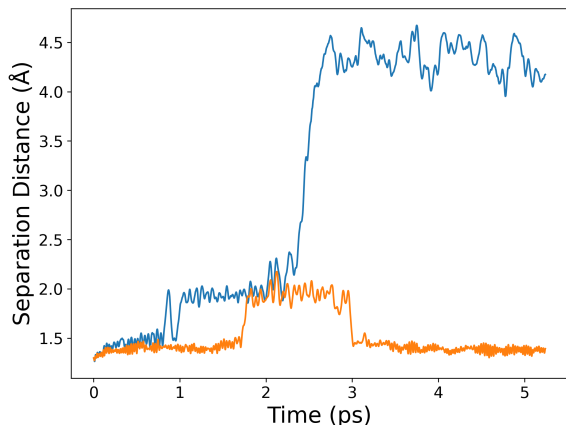


Figure S2: Separation distance between the atoms of each of the two initial O_2 molecules across simulation time.

The second of these systems was created by adding three additional replicas, quadrupling the system size. The ORR was observed for one O_2 molecules within 700 fs of simulation (Figure S3).

Distribution of Electron Holes

In table S1 we show the distribution of holes between different carbon neighbors with respect to central nitrogen. These populations are averages across all "X-Neighbor" carbon atoms for all nitrogen atoms over the 1.5 to 2.0 ps simulation time-frame.

In Figure S4 we show different possible electron hole creation scenarios. Upon single-electron injection, a radical and a carbocation will be formed. If the carbocation is formed in the first neighbor, it can then be delocalized across all the other odd neighbors. To explain

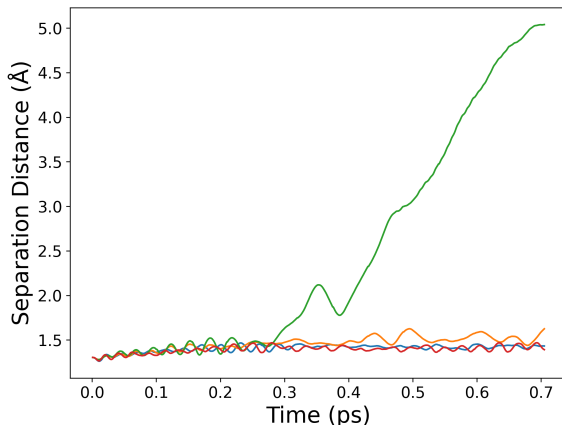


Figure S3: Separation distance between the atoms of each of the four initial O_2 molecules across simulation time.

Table S1: Mulliken population average during simulation time from 1.5 to 2.0 ps showing the distribution of electron holes. First-neighbor carbon atoms have the largest negative Mulliken population average, suggesting that electrons are primarily removed from those atoms. Smaller negative Mulliken populations on third-neighbor carbons and beyond suggest that additional positive charge on the oxidized NG sheet can be delocalized to positions beyond the first-neighbor as well, though to a lesser degree.

Selected Atoms	Average Mulliken Population from 1.5 ps to 2.0 ps
Nitrogen Atoms	0.093
First-Neighbor Carbon Atoms	-0.202
Second-Neighbor Carbon Atoms	0.019
Third-Neighbor Carbon Atoms	-0.035
Fourth-Neighbor Carbon Atoms	-0.015
Fifth-Neighbor Carbon Atoms	-0.034
Sixth-Neighbor Carbon Atoms	-0.019

positive charge in the second neighbors (and all the even neighbors), one has to propose either a second carbocation formation or a structure as in the bottom left corner of Figure S4. Note that in the case where the carbocation is formed in the second neighbor, it will certainly lead to a more strained and unstable structure. The latter could explain why there is no clear evidence that the positive charge is localized in the second neighbor position, as evidenced in Table S1.

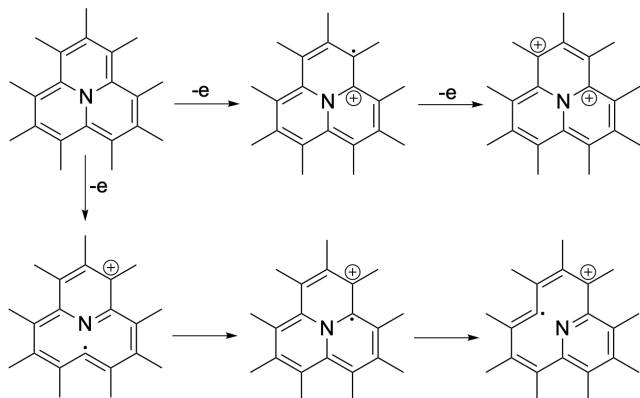


Figure S4: Possible resonance structures to explain the localization of the holes (positive charges) on the carbon atoms surrounding nitrogen doping atoms in the N-doped graphene catalyst. These resonance structures show additional possibilities to those proposed in the main text, including how charge might be delocalized to have a positive charge on both even- and odd-neighboring carbon atoms.

Chemical Potentials for Full System and Subsystems

Table S2 shows the electron chemical potential for different sub-components of the system. It is important to highlight the difference between pure carbon graphene and N-doped graphene with respect to water. There are more than 0.5 eV differences when comparing the two materials. We see that NG is higher than pure graphene, which is one plausible explanation for why we see reduction only in the case of NG at least for the simulated timescales.

Table S2: Chemical potential (μ) values for the full simulation system ("All") and various subsystems

Subsystem	μ
All	-3.658
N-Doped Graphene	-3.072
O ₂	-6.469
Water	-6.326
Pure Carbon Graphene	-3.698